Rapid on-site nondestructive surface corrosion characterization of sintered nanocopper paste in power electronics packaging using hyperspectral imaging

Chen, Wei; Feng, Shuo; Liu, Xu; Hu, Dong; Zhu, Xi; Yao, Qi; Fan, Xuejun; Zhang, Guoqi; Fan, Jiajie

DOI
10.1016/j.microrel.2024.115508

Publication date
2024

Document Version
Final published version

Published in
Microelectronics Reliability

Microelectronics Reliability 162 (2024) 115508

Contents lists available at ScienceDirect

Microelectronics Reliability

journal homepage: www.elsevier.com/locate/microrel

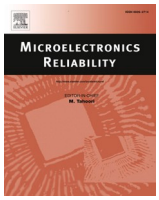

Rapid on-site nondestructive surface corrosion characterization of sintered nanocopper paste in power electronics packaging using hyperspectral imaging

Wei Chen [a], Shuo Feng [a], Xu Liu [a], Dong Hu [b], Xu Liu [b], Xi Zhu [c], Qi Yao [a], Xuejun Fan [d], Guoqi Zhang [b], Jiajie Fan [a,b,c,*]

[a] Institute of Future Lighting, Academy for Engineering & Technology, Shanghai Engineering Technology Research Center for SiC Power Device, Fudan University, Shanghai 200433, China
[b] EEMCS Faculty, Delft University of Technology, Delft 2628, the Netherlands
[c] Research Institute of Fudan University in Ningbo, Ningbo 315336, China
[d] Department of Mechanical Engineering, Lamar University, PO Box 10028, Beaumont, TX 77710, USA

ARTICLE INFO

Keywords:
Power electronics packaging
Sintered nanocopper
H_2S corrosion
Hyperspectral imaging
Tarnishing products

ABSTRACT

Sintered nanocopper (nanoCu) paste, exhibiting excellent electrical, thermal, and mechanical performances, offers promise for interconnections in wide bandgap (WBG) semiconductors operating at higher temperatures. However, sintered nanoCu is prone to severe corrosion in environments containing H_2S, with on-site characterization methods for the composition of corrosion products currently lacking. In this study, a novel method was proposed for the rapid characterization of corrosion products during the corrosion process based on hyperspectral imaging (HSI) technology. Sintered nanoCu samples were subjected to 336 h H_2S gas corrosion tests with bulk Cu as the reference, followed by correlating the corrosion element content with hyperspectral characteristic parameters. Then, the morphology and composition of corrosion products were researched using focused ion beam scanning electron microscope (FIB-SEM) and transmission electron microscope (TEM) analysis. The results showed that (1) during the corrosion process, a linear relationship was established between the Cu, O elemental atomic contents on the sample surfaces and their hyperspectral characteristic parameters. (2) The elemental atomic content of S exhibited an exponential relationship with the characteristic parameter. (3) The change rate in the spectral characteristic parameters during the corrosion process reflected the severity of corrosion, which was confirmed by comparing the thickness of the corrosion products of the sintered nanoCu and bulk Cu. This study offers a foundation for the further investigation of rapid on-site characterization of sintered nanoCu corrosion involving H_2S.

1. Introduction

In recent years, power semiconductor devices have gained significant attention from the electronic industry by enabling power conversion and circuit control [1–3]. Power device packaging technology has progressed toward higher frequencies, faster response times, greater integration, improved power conversion efficiency, and higher operational junction temperatures [4–6]. Sintered nanoCu, with low processing temperatures and a high melting point, can adapt well to the high operational temperatures of wide bandgap (WBG) semiconductors [7,8], showing promise for chip interconnection in WBG semiconductors [9–11]. In addition, due to its exceptional electrical and thermal conductivity, as well as favorable processability, Cu has shown extensive application in lead frames, substrates, bonding wires, micro-bumps, and various structural components in advanced electronic packaging [6,12–15].

Sintered nanoCu and bulk Cu pose potential reliability issues such as corrosion degradation, when employed in electronic packaging [16].

* Corresponding author at: Institute of Future Lighting, Academy for Engineering & Technology, Shanghai Engineering Technology Research Center for SiC Power Device, Fudan University, Shanghai 200433, China.
E-mail addresses: chenw21@m.fudan.edu.cn (W. Chen), 21210860045@m.fudan.edu.cn (S. Feng), 22210860075@m.fudan.edu.cn (X. Liu), D.Hu@tudelft.nl (D. Hu), liux32019@mail.sustech.edu.cn (X. Liu), yaoqi@fudan.edu.cn (Q. Yao), xfan@lamar.edu (X. Fan), G.Q.Zhang@tudelft.nl (G. Zhang), jiajie_fan@fudan.edu.cn (J. Fan).

https://doi.org/10.1016/j.microrel.2024.115508
Received 23 June 2024; Received in revised form 11 August 2024; Accepted 16 September 2024
Available online 24 September 2024

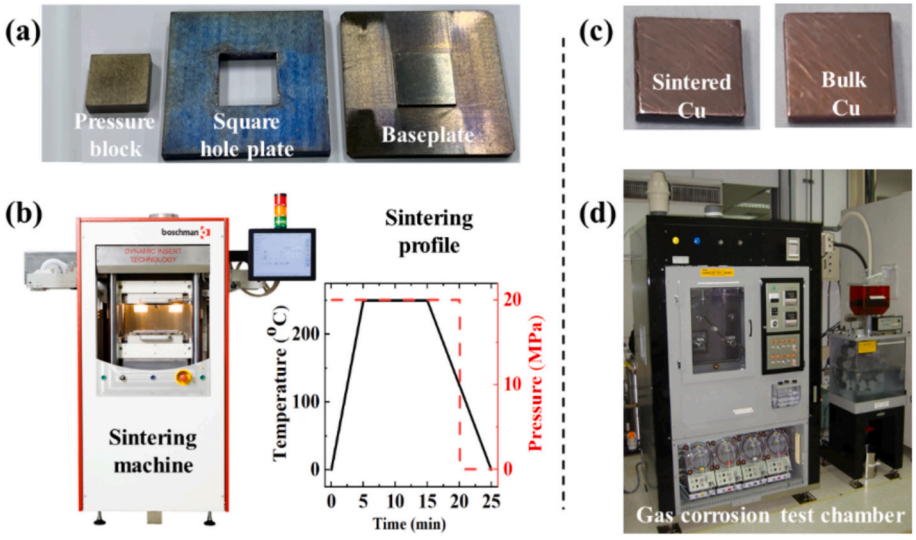

Fig. 1. (a) Self-designed square-shaped mold; (b) sintering machine and temperature profile; (c) sintered nanoCu and bulk Cu samples images; (d) gas corrosion test chamber.

Environmental corrosion stress can significantly impact chip interconnection, making it a vulnerable point prone to failure [17–19]. Sintered nanoCu will be susceptible to severe corrosion degradation when confronted by harsh operating environments such as offshore wind power applications, especially those involving combined stresses such as high pressure, high temperature, high humidity, and intense H_2S corrosion [8,20]. Corrosive gases like H_2S, found in coastal and offshore areas, can cause severe corrosion of sintered Cu interconnectors, resulting in the degradation of their electrical, thermal, and mechanical properties [21,22]. Therefore, developing an efficient and precise corrosion product characterization method is critical for understanding and preventing corrosion in metal interconnect materials.

Prevalent techniques for corrosion products characterization currently include X-ray powder diffraction (XRD) [23,24], X-ray photoelectron spectroscopy (XPS) [25], scanning electron microscopy combined with energy-dispersive X-ray spectroscopy (SEM-EDS) [26], Fourier transform infrared spectroscopy (FTIR) [27], and Raman spectroscopy [28]. However, these methods have shown to be primarily effective in identifying aging products under atmospheric corrosion within controlled laboratory settings and have limitations when applied outside these conditions due to time-consuming procedures and inherent challenges. By contrast, hyperspectral imaging (HSI) has emerged as a promising tool for simultaneous spatial and spectral inspection, as it can provide RGB information and surface composition details based on distinct wavelength responses [29,30]. This technology may serve as a potential solution for material composition characterization beyond the constraints encountered when utilizing traditional methods.

Numerous studies have focused on utilizing hyperspectral information across various wavelength ranges, to investigate the corrosion products and degree of corrosion in metals [31–34]. Ma et al. [31] proposed a technique that leveraged the reflectance spectral responses of coatings, spanning from the visible to near-infrared (VNIR, 400–100 nm) range, to determine the condition of steel beam coatings. This underscored the swift and dependable capability of HSI in detecting corrosion in metal coatings. Zahir et al. [32] demonstrated that high spectral data in the shortwave infrared (SWIR, 1100–1700 nm) range could be used to detect the type and degree of corrosion in carbon steel samples. Subsequently, the study employed reference spectra to monitor the temporal variations of different corrosion products (goethite, magnetite, lepidocrocite, and hematite) in the carbon steel samples [33]. Ktash et al. [34] utilized HSI reflectance spectroscopy within the ultraviolet (UV, 200–380 nm) range to non-destructively and rapidly characterize the Cu oxidation state and layer thickness on direct bonded copper (DBC). Liggins et al. [35] merged HSI with unsupervised machine learning algorithms to automate spectral clustering, presenting a high-resolution SWIR imaging solution for the rapid detection of corrosion products in ancient bronze.

Many studies have also focused on employing HSI to address the detection and screening issues of other materials [33–38]. Tao et al. [36] proposed a method for employing HSI and machine learning models to characterize and classify urban solid waste. The researchers achieved nearly 100 % accuracy under specific parameter conditions, and effectively identified inorganic components within waste. Pu et al. [37] combined HSI with convolutional neural networks (CNNs) to distinguish between fresh and freeze-thawed beef samples, offering a potential non-destructive tracing method for diverse beef conditions. Extracting key information from spectral patterns enabled principal component analysis, while artificial neural networks demonstrated exceptional classification and regression performance. Zhou et al. [38] used HSI for the visual non-destructive detection of composite heavy metals in lettuce leaves. The researchers preprocessed hyperspectral data using techniques such as multi-scatter correction and variable iterative space shrinkage, establishing a model to detect composite heavy metal content.

However, a comprehensive understanding of the corrosion behavior of sintered nanoCu relying on HSI in H_2S-containing environments has remained insufficient. In this study, gas corrosion experiments involving H_2S were conducted on sintered nanoCu and bulk Cu samples, followed by HSI to detect samples at various stages of corrosion. Subsequently, a correlation between hyperspectral characteristic parameters and element content was established through combined XPS analysis. Finally, the corrosion phenomena and product composition of the samples were analyzed based on FIB-SEM and TEM. This manuscript was structured as follows. Section 2 introduces the preparation of samples and experimental test settings, Section 3 investigates the variation patterns of hyperspectral data during the corrosion process, the relationship between hyperspectral characteristic parameters and element content in the corrosion products, as well as the corrosion phenomena and mechanisms, and Section 4 summarizes the study.

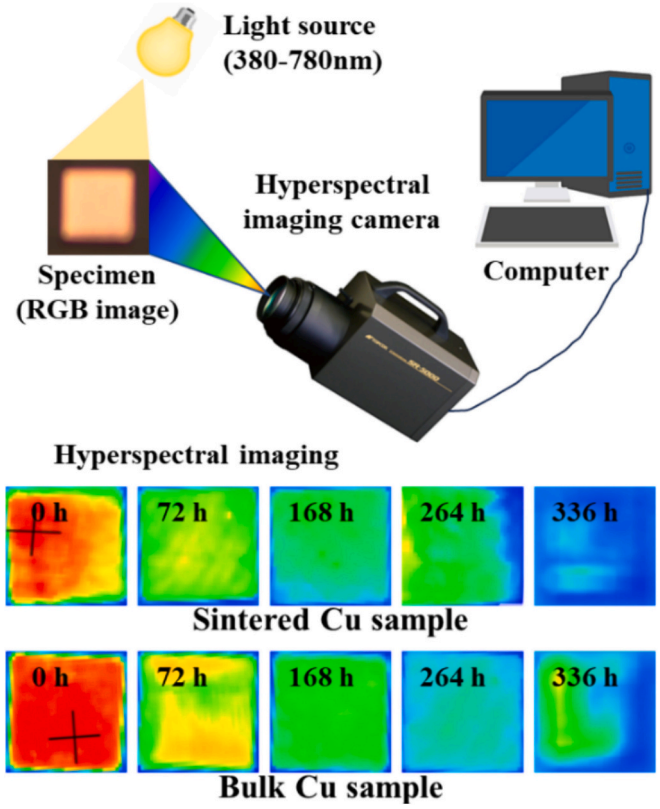

Fig. 2. Schematic diagram of the HSI test.

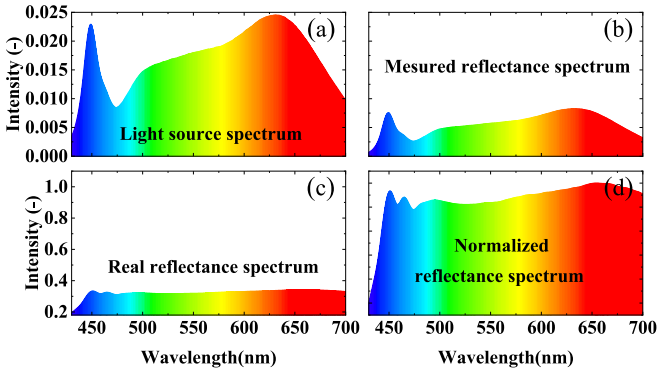

Fig. 3. The spectral data involved in the data processing procedure: (a) light source spectrum; (b) measured reflectance spectrum; (c) real reflectance spectrum and (d) normalized reflectance spectrum.

2. Experimental details

2.1. Sample preparation and gas corrosion test

In this study, sintered nanoCu and bulk Cu samples, each measuring 5 × 5 × 1 mm in size, were used to investigate the corrosion processes involving H_2S. The Cu nanoparticle paste was composed of Cu nanoparticles (average particle size of 150–300 nm), ethylene glycol (99.5 %, Aladdin Reagent Co., Ltd.), and terpinol (95.0 %, Aladdin Reagent Co., Ltd.). A custom-designed square-shaped mold was used to produce the sintered nanoCu samples (Fig. 1 (a)). The Cu nanoparticle paste was first injected into the mold, then preheated at 120 °C for 30 min in a vacuum oven (DZF-6012, YIHENG). This was followed by pressure-assisted sintering in a nitrogen atmosphere using an industrial standard sintering machine (Sinterstar Innovate-F-XL, Boschman) at 250 °C and 20 MPa for 25 min. The sintering machine and temperature profile are shown in Fig. 1 (b). The bulk Cu samples were procured from SHENG SHI JING New Material Co., Ltd., China. Fig. 1 (c) shows the sintered nanoCu and bulk Cu samples.

To assess the impact of H_2S on corrosion, a 336 h aging test was conducted on both the sintered and bulk samples within a commercial gas corrosion test chamber (GH-180, YAMASAKI) (Fig. 1 (d)). The test conditions included a temperature of 45 °C, relative humidity of 85 %, and an H_2S concentration of 1 ppm. Before H_2S exposure, the surfaces of all sintered and bulk Cu samples were polished using 4000-grit sandpaper. At 168 h intervals, 10 sintered nanoCu samples and 10 bulk Cu samples were extracted for inspection.

2.2. Hyperspectral imaging system

Fig. 2 illustrates the HSI system, which was comprised of a light source, samples, a hyperspectral camera (SR-5000, TOPCON), and a computer. The reflectance spectrum of the light source (380–440 nm) on the samples was captured using a calibrated hyperspectral camera. The hyperspectral image was displayed on a computer with pre-installed software, generating an image data cube. The image cube with a resolution of 1.4 million (1376 × 1024) was acquired, signifying that the spectral data (ranging from 380 to 780 nm, with a 1 nm interval) were obtained for each pixel point. Adjustments were made upon the integration time during measurement to obtain smooth and continuous spectra. Measurements were conducted in a darkroom with uniform illumination to minimize stray light interference.

2.3. Characterization methodology

The optical microscope (OM) (BX53M, OLYMPUS) was used to capture the surface information of the sintered samples to examine the aging-induced changes in the macro-topography. The elements in the corrosion products were investigated by XPS (Axis Supra+, SHIMADZU) with an Al Kα excitation source (hv = 1486.6 eV). TEM (JEM-F200, JEOL) was performed on the samples to further analyze the morphology and composition of the corrosion products. The TEM samples were prepared by performing cross-sectional cuts and analysis on the samples using a FIB-SEM (Crossbeam 550, ZEISS).

3. Results and discussions

3.1. Spectrum feature

To obtain the reflectance spectral features of the samples, hyperspectral experiments were conducted on samples subjected to different corrosion times. The measured reflectance spectrum on the sample is depicted in Fig. 3 (a), indicating features inherited from the light source spectrum (see Fig. 3 (b)). To mitigate the shape influence of the light source spectrum, mathematical operations were required for the measured reflectance spectrum, as described by Eq. (1):

$$\lambda_{real}(i) = \frac{\lambda_{measured}(i)}{\lambda_{light}(i)}, \tag{1}$$

where $\lambda_{real}(i)$, $\lambda_{measured}(i)$, and $\lambda_{light}(i)$ represent the real reflectance spectrum, measured spectrum, and light source spectrum, respectively, and i denotes the wavelength. The real reflectance spectrum is depicted in Fig. 3 (c). In the hyperspectral experiments, the position variations could influence the intensity of the real reflectance spectrum of the sample. To eliminate this effect, normalization of the real reflectance spectrum was required, using the specific approach outlined in Eq. (2):

$$\lambda_{normalized}(i) = \frac{\lambda_{real}(i) - \lambda_{\max}}{\lambda_{\max} - \lambda_{\min}}, \tag{2}$$

where $\lambda_{normalized}(i)$ represents the normalized real reflectance spectrum,

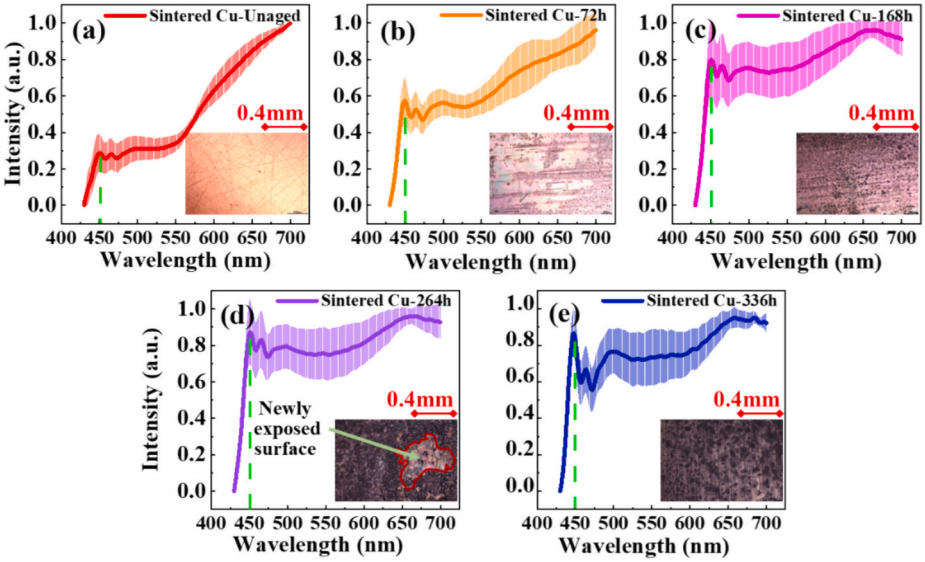

Fig. 4. The average reflectance spectra (solid line) and their standard deviation (shaded area) obtained from 10 spectral acquisition areas on each of the 6 sintered nanoCu samples: (a) unaged sintered nanoCu samples; (b) sintered nanoCu samples after 72 h of corrosion; (c) sintered nanoCu samples after 168 h of corrosion; (d) sintered nanoCu samples after 264 h of corrosion; (e) sintered nanoCu samples after 336 h of corrosion.

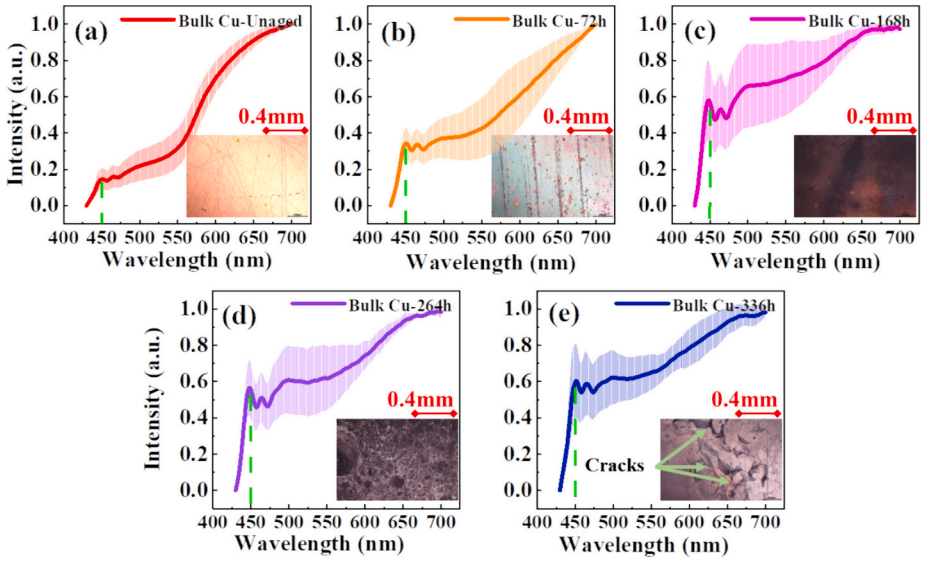

Fig. 5. The average reflectance spectra (solid line) and their standard deviations (shaded area) obtained from 10 spectral acquisition areas on each of the 6 bulk Cu samples: (a) unaged bulk Cu samples; (b) bulk Cu samples after 72 h of corrosion; (c) bulk Cu samples after 168 h of corrosion; (d) bulk Cu samples after 264 h of corrosion; (e) bulk Cu samples after 336 h of corrosion.

and λ_{max} and λ_{min} denote the maximum and minimum intensities within $\lambda_{real}(i)$. Fig. 3 (d) shows the normalized real reflectance spectrum.

Both sintered nanoCu and bulk Cu were subjected to corrosion over 5 time periods: 0, 72, 168, 264, and 336 h. Hyperspectral experiments were conducted on the samples under different corrosion durations, with 6 samples for each corrosion duration. Ten circular regions were selected at the four corners and central position on the surface of each sample, and the hyperspectral data (440–780 nm; 1 nm interval) were collected from each of these circular regions. In addition, the surface morphologies of the samples were captured using OM.

Fig. 4 shows the average reflectance spectra of the sintered nanoCu samples with different corrosion times, with the insets showing the surface morphology images of the corresponding samples. According to the OM images, we observed that with an increase in corrosion time, the color of the sintered nanoCu samples changed from yellow to black-brown. The corrosion products demonstrated a layered morphology, and after 264 h of corrosion, the corrosion product film on the surface of the sintered nanoCu sample peeled off, revealing a new surface. Following 336 h of corrosion, the newly exposed surface was again covered by corrosion products. The reflectance spectra of the sintered nanoCu samples also changed with an increase in corrosion time, and the standard deviation of the samples demonstrated an increasing trend. A characteristic peak appeared in the reflectance spectra at 450 nm, which continuously increased with increasing corrosion time. The corrosion products formed in H_2S environment are sensitive to light at a wavelength of 450 nm and exhibit high emission efficiency at this wavelength. As the quantity of corrosion products increases, the intensity of reflected light at 450 nm also rises.

Fig. 5 shows the average reflectance spectra of the bulk Cu samples, with the inset figures showing the surface morphology images of the

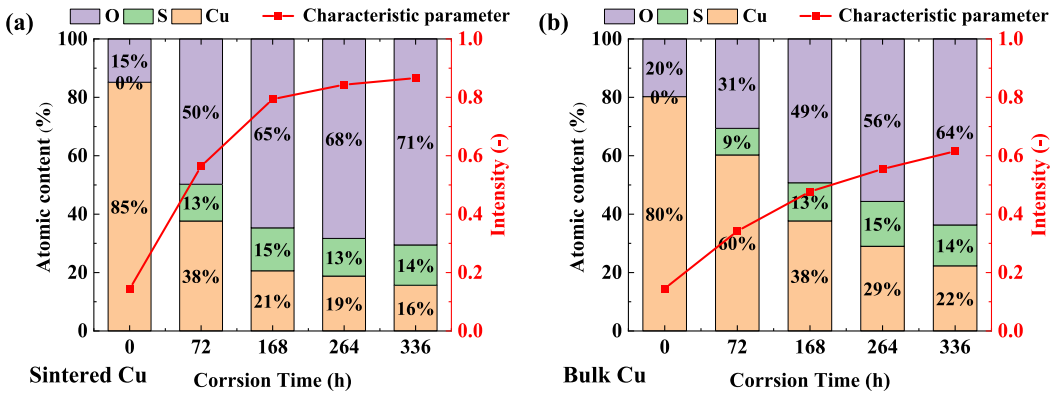

Fig. 6. Elemental contents and characteristic parameter changes with corrosion time: (a) sintered nanoCu; (b) bulk Cu.

Table 1
Fitting results obtained by using the linear function.

Parameters	Element	*a*	*b*	R^2
Sintered nanoCu	Cu	−95.02	96.59	0.9879
	O	76.28	4.68	0.9987
Bulk Cu	Cu	−132.49	102.00	0.9844
	O	95.33	3.12	0.9712

Table 2
Fitting results obtained by using the exponential function.

Parameters	Element	P_1	P_2	P_3	R^2
Sintered nanoCu	S	−31.14	250.22	14.08	0.9881
Bulk Cu	S	−31.47	47.73	17.85	0.9843

samples. With an increase in corrosion time, the color of the bulk Cu samples also changed from yellow to black-brown, and the corrosion products exhibited a layered morphology. No peeling of the corrosion product film was observed in the samples for all corrosion times, and only the cracks in the corrosion product film were found in the sample following 336 h of corrosion. A characteristic peak also appeared in the reflectance spectra of the bulk Cu samples at 450 nm, which continuously increased with increasing corrosion time, however, the increase magnitude was smaller than the sintered nanoCu samples. These demonstrated that the sintered nanoCu underwent more severe corrosion than bulk Cu. The sintered sample with voids presented a larger surface area, making it more susceptible to corrosive gas reactions, and facilitating the easier penetration of corrosive gas into the interior of the sintered sample.

3.2. Tarnishing product characterization

The elemental contents in the samples with different corrosion times were assessed by XPS. The intensity of the characteristic peak at 450 nm in the reflectance spectra was defined as the characteristic parameter. Fig. 6 presents the elemental content trends and characteristic parameters of the sintered nanoCu and bulk Cu samples with different corrosion times, respectively. For sintered nanoCu, the surfaces of the unaged samples contained oxygen (O) elements, because the Cu elements were easily oxidized to copper (I) oxide and copper (II) oxide in the air [39]. In the corrosion experiment, sulfur (S) elements appeared on the sample surfaces, however, the S content remained stable and did not significantly change with the corrosion time. The change rates of Cu and O were high during the first 168 h of corrosion and then slowed down significantly. The characteristic parameters also showed an initial rapid increase (0–168 h) followed by a slower rate of increase (168–336 h). For the unaged bulk Cu samples, the surface revealed the presence of O elements, while S elements were detected in the aged samples, and S content displayed fluctuations. Similarly, the Cu and O elements on the bulk Cu samples decreased and increased, respectively, during corrosion, at a slower rate than sintered nanoCu. Throughout the corrosion process, the change rate of Cu and O content for the bulk Cu samples remained relatively steady. Correspondingly, the characteristic parameters of the bulk Cu samples demonstrated a gradual increase trend throughout the corrosion process.

Analysis revealed a clear correlation between the characteristic pa-

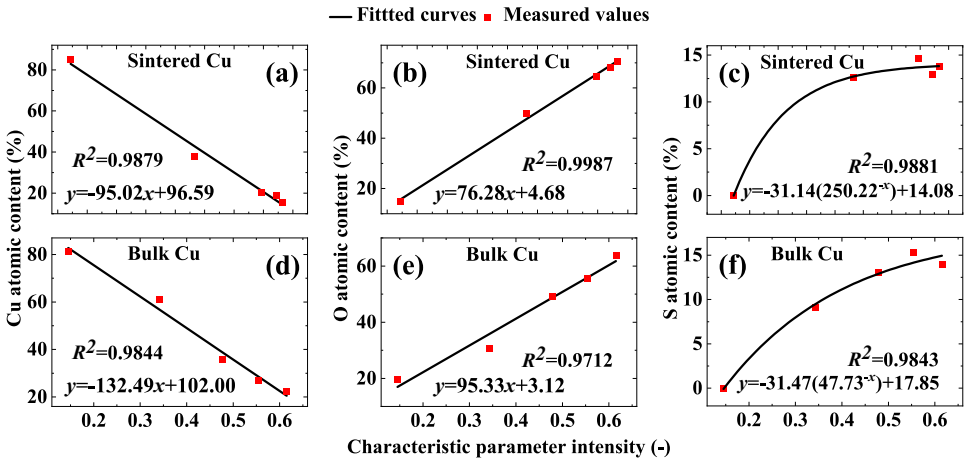

Fig. 7. The measured values and fitted curves of elemental atomic content versus characteristic parameter: (a) Cu within sintered nanoCu sample; (b) O within sintered nanoCu sample; (c) S within sintered nanoCu sample; (d) Cu within bulk Cu sample; (e) O within bulk Cu sample; (f) S within bulk Cu sample.

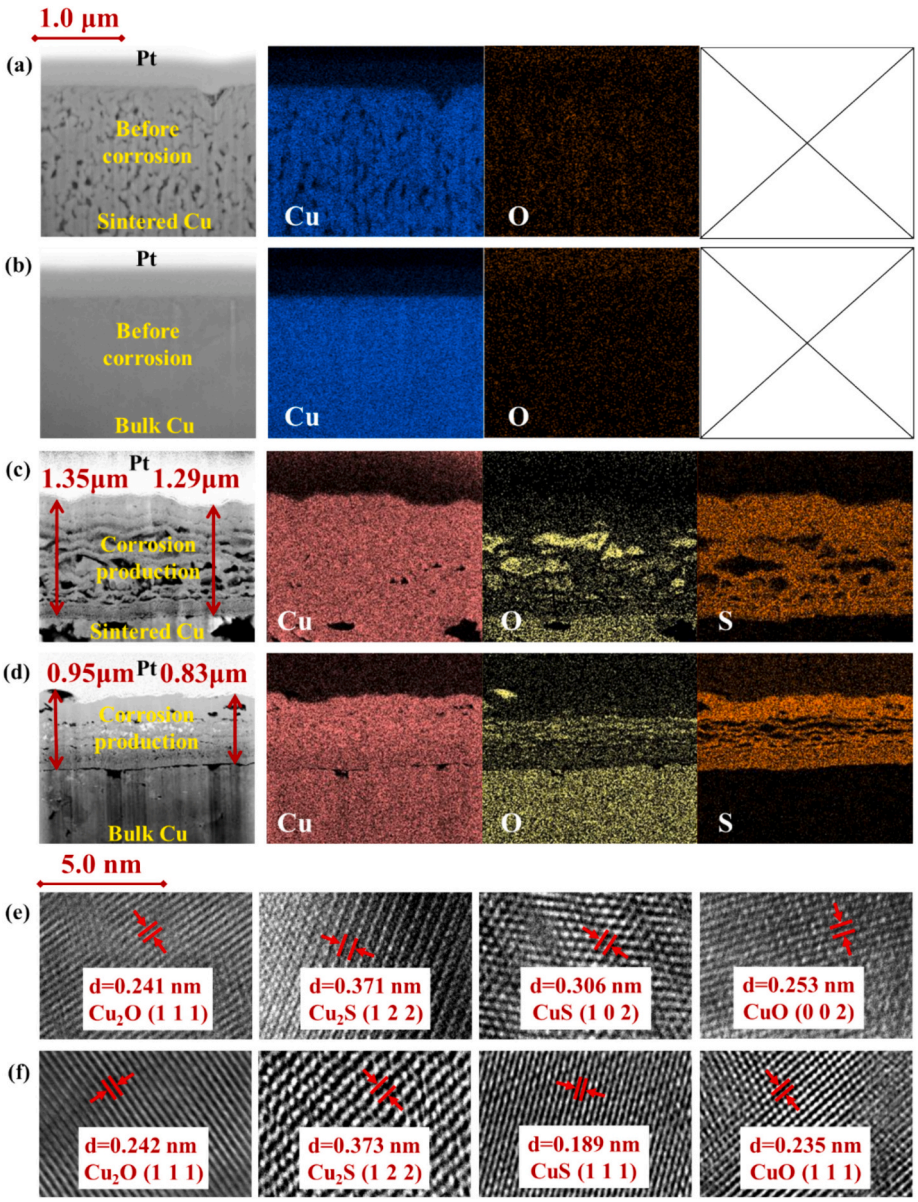

Fig. 8. FIB, TEM/EDS and HRTEM results of different samples: (a) FIB and TEM/EDS results of sintered nanoCu sample before corrosion; (b) FIB and TEM/EDS results of bulk Cu sample before corrosion; (c) FIB and TEM/EDS results of sintered nanoCu sample subjected to 336 h of corrosion; (d) FIB and TEM/EDS results of Bulk Cu sample subjected to 336 h of corrosion; (e) HRTEM results of sintered nanoCu sample subjected to 336 h of corrosion and (f) HRTEM results of bulk Cu sample subjected to 336 h of corrosion.

rameters and Cu, O and S atomic contents in both the sintered and bulk Cu samples. To elucidate those relationships, a linear function (Eq. (3)) was used to fit the variations in both Cu and O atomic contents concerning the characteristic parameter:

$$y = ax + b, \tag{3}$$

where a and b denote the parameters within the linear function. An exponential function (Eq. (5)) was utilized to accurately represent the correlation between the atomic content of S element and the characteristic parameter:

$$y = p_1 \times (p_2{}^{-x}) + p_3, \tag{4}$$

where p_1, p_2, and p_3 denote the parameters within the quadratic function. The coefficient of determination (R^2 value) has been commonly used to indicate the goodness of fit of a regression model, as calculated by the following equation [40]:

$$R^2 = 1 - \frac{\sum (y_i - \hat{y}_i)^2}{\sum (y_i - \bar{y})^2}, \tag{5}$$

where y_i represents the i^{th} measured value, $\hat{y}_i$ denotes the i^{th} fitted value, and $\bar{y}$ represents the average value of all measured values.

The model parameters for Cu and O atomic contents were extracted by linear fitting using particle swarm optimization (PSO) conducted in 1stOpt software, as listed in Table 1; the exponential function parameters for S are listed in Table 2. The measured and fitted values of Cu, O and S atomic contents in both the sintered and bulk Cu are presented in Fig. 7. The slope of the fitted equation for Cu element in the sintered samples was lower than that in the bulk samples, indicating a more severe level of corrosion in the sintered samples.

As shown in Fig. 7 (a), (b), (d) and (e), a strong agreement was achieved between the measured and fitted Cu and O atomic contents through high R^2 values for both the sintered and bulk Cu samples.

Consequently, a strong linear correlation was evident between the characteristic parameter and the atomic contents of Cu and O. Fig. 7 (c) and (f) illustrate a strong agreement between measured and fitted S atomic contents for both sintered and bulk copper samples, indicating a significant exponential relationship between the Cu atomic content and the characteristic parameter. Thus, employing Eqs. (3) and (4) allowed for the computation of elemental content in the sample corrosion products, leveraging easily accessible spectral characteristics.

3.3. Corrosion mechanism analysis

The cross-sections of the sintered and bulk Cu samples before corrosion were obtained using FIB cutting. The cross-sections, along with the TEM/EDS test results for both sintered and bulk Cu, are shown in Fig. 8 (a) and (b). The figures reveal that the sintered Cu sample contains some voids, while the bulk Cu exhibits a dense structure. The cross-sections of the corrosion product films at the central positions of the sintered and bulk Cu samples, which were subjected to 336 h of corrosion, were obtained through FIB cutting. To ensure the integrity of the corrosion product films, a layer of platinum (Pt) metal was deposited on the central region of the sample surfaces before FIB cutting occurred. The cross-sections generated by FIB and test results from the TEM/EDS of both the sintered and bulk Cu are shown in Fig. 8 (c) and (d). After 336 h of corrosion, the corrosion product films on the sintered nanoCu and bulk Cu samples measured approximately 1.32 and 0.89 μm, respectively. Both samples exhibited distinct interfaces between the corrosion product layers and the Cu matrix. The sintered nanoCu sample displayed a few voids in its Cu matrix, resulting in a relatively porous corrosion product layer. By contrast, the bulk Cu sample exhibited a denser corrosion product layer due to the absence of porosity in its Cu matrix. The corrosion product layers in both the sintered and bulk samples consisted of Cu, O, and S elements, which was consistent with previous XPS findings. The O content in the corrosion product film was lower than that in the Cu matrix. S existed exclusively within the corrosion product film and was not present within the Cu matrix, with a clear border observed between Cu matrix and S element. Therefore, it was inferred that O initially reacted with the Cu matrix to form Cu oxides, followed by H_2S reacting with the Cu oxides to produce sulfides.

The corrosion products of the samples were examined by TEM, and the high-resolution TEM (HRTEM) images of both the sintered nanoCu and bulk Cu, subjected to 336 h of corrosion, are shown in Fig. 8 (e) and (f). For sintered nanoCu, four distinct lattice spacings were observed in the corrosion products, measuring 0.241 nm, 0.371 nm, 0.306 nm, and 0.253 nm, as obtained by the Joel Gatan Microscopy Suite 3.0 (GSM 3.0). These four distances corresponded to the crystallographic planes of Cu_2O (1 1 1) (PDF: 34-1354), Cu_2S (1 2 2) (PDF: 33-0490), CuS (1 0 2) (PDF: 06-0464), and CuO (0 0 2) (PDF:48-1548). The bulk Cu sample also displayed four distinct lattice spacings, measuring 0.242 nm, 0.373 nm, 0.189 nm, and 0.235 nm, corresponding to the crystallographic planes of Cu_2O (1 1 1) (PDF: 34-1354), Cu_2S (1 2 2) (PDF: 33-0490), CuS (1 1 1) (PDF: 06-0464), and CuO (1 1 1) (PDF: 48-1548), respectively. Under the atmospheric conditions of 45 °C, 85 % humidity, and 1 ppm H_2S, both sintered nanoCu and bulk Cu generated four main corrosion products, namely, Cu_2O, Cu_2S, CuO, and CuS.

4. Conclusions

In this study, a sintered nanoCu sample was prepared using nano-copper paste and subjected to 336 h of corrosion aging in an environment containing 1 ppm H_2S, with bulk Cu as a reference. Subsequently, the hyperspectral data for the sintered nanoCu and bulk Cu samples were acquired by an HSI system. During the corrosion process, the relationships between the hyperspectral characteristic parameters and elemental compositions on the sample surfaces was analyzed. Finally, the sample composition was determined. The results revealed that (1) the average reflectance spectra of the samples were calculated using computational methods, revealing systematic changes during corrosion. (2) A linear relationship was found between the Cu, O atomic surface contents and the spectral characteristics at 450 nm; besides, the elemental atomic content of S exhibited an exponential relationship with the characteristic parameter. (3) A more rapid increase in characteristic parameters signified severe corrosion in the samples. The corrosion product thickness of the sintered nanoCu sample, which demonstrated a faster increase in characteristic parameters, was approximately 1.32 μm, while that of the bulk Cu sample, with a slower increase, was about 0.89 μm. (4) Both the sintered and bulk Cu samples produced Cu_2O, Cu_2S, CuO, and CuS in an environment containing H_2S, as confirmed by the TEM results; And O initially reacts with Cu to form oxides, followed by the reaction of H_2S with Cu oxides to produce sulfides. This study introduced a rapid characterization method for sintered nanoCu corrosion, offering the potential to advance the application of sintered nanoCu interconnections in WBG semiconductors. The relationship between different types of corrosion products and their surface reflection spectra will be analyzed in the future study.

Declaration of competing interest

The authors declare that they have no known competing financial interests or personal relationships that could have appeared to influence the work reported in this paper.

Data availability

Data will be made available on request.

Acknowledgments

This work was supported by National Natural Science Foundation of China (No. 52275559).

References

[1] Z. Sun, Y. Wang, M. Li, Y. Guan, D. Xu, Analysis and design of 6.78M WPT architecture for configurable power applications based on DCX energy synthesis and functional execution, IEEE Trans. Power Electron. 39 (1) (2024) 106–111.
[2] A. Kumar, M. Moradpour, M. Losito, W.-T. Franke, S. Ramasamy, R. Baccoli, G. Gatto, Wide band gap devices and their application in power electronics, Energies 15 (23) (2022) 9172.
[3] B. Shi, A.I. Ramones, Y. Liu, H. Wang, Y. Li, S. Pischinger, J. Andert, A review of silicon carbide MOSFETs in electrified vehicles: application, challenges, and future development, IET Power Electron. 16 (12) (2023) 2103–2120.
[4] J. Hu, Y. Shan, K.W. Cheng, S. Islam, Overview of power converter control in microgrids—challenges, advances, and future trends, IEEE Trans. Power Electron. 37 (8) (2022) 9907–9922.
[5] S. Jones-Jackson, R. Rodriguez, Y. Yang, L. Lopera, A. Emadi, Overview of current thermal management of automotive power electronics for traction purposes and future directions, IEEE Transactions on Transportation Electrification 8 (2) (2022) 2412–2428.
[6] W. Chen, J. Jiang, A.H. Meda, M.S. Ibrahim, G. Zhang, J. Fan, A thin and low-inductance 1200 V SiC MOSFET fan-out panel-level packaging with thermal cycling reliability evaluation, IEEE Trans. Electron Devices 70 (5) (2023) 2268–2275.
[7] T.F. Chen, K.S. Siow, Comparing the mechanical and thermal-electrical properties of sintered copper (Cu) and sintered silver (Ag) joints, J. Alloys Compd. 866 (2021) 158783.
[8] X. Wang, Z. Yang, B. Wang, W. Chen, G. Zhang, J. Zhang, J. Fan, P. Liu, Effect of epoxy resin addition on properties and corrosion behavior of sintered joints in power modules serviced offshore, J. Mater. Res. Technol. 25 (2023) 6593–6612.
[9] X. Liu, S. Li, J. Fan, J. Jiang, Y. Liu, H. Ye, G. Zhang, Microstructural evolution, fracture behavior and bonding mechanisms study of copper sintering on bare DBC substrate for SiC power electronics packaging, J. Mater. Res. Technol. 19 (2022) 1407–1421.
[10] W.Y. Li, C.T. Chen, M. Ueshima, T. Kobatake, K. Suganuma, Large area bare Cu-Cu interconnection using micro-Cu paste at different sintering temperatures and pressures, Microelectron. Reliab. 150 (2023) 115105.
[11] D.-P. Tran, Y.-T. Liu, C. Chen, Effects of Cu/SnAgCu powder fraction and sintering time on microstructure and mechanical properties of transient liquid phase sintered joints, Materials 17 (9) (2024) 2004.
[12] L. Wang, T. Zhang, F. Yang, D. Ma, C. Zhao, Y. Pei, Y. Gan, Cu clip-bonding method with optimized source inductance for current balancing in multichip SiC MOSFET power module, IEEE Trans. Power Electron. 37 (7) (2022) 7952–7964.

[13] Z. Huang, Y. Li, L. Chen, Y. Tan, C. Chen, Y. Kang, F. Luo, A novel low inductive 3D SiC power module based on hybrid packaging and integration method, in: 2017 IEEE Energy Conversion Congress and Exposition (ECCE), 2017, pp. 3995–4002.
[14] W. Mu, L. Wang, B. Wang, T. Zhang, F. Yang, Y. Gan, H. Zhang, Direct integration of optimized phase-change heat spreaders into SiC power module for thermal performance improvements under high heat flux, IEEE Trans. Power Electron. 37 (5) (2022) 5398–5410.
[15] K.-C. Shie, P.-N. Hsu, Y.-J. Li, D.-P. Tran, C. Chen, Failure mechanisms of Cu–Cu bumps under thermal cycling, Materials 14 (19) (2021) 5522.
[16] J. Alptekin, K.A.J. Durai, D.K. Kumaravel, L. Estridge, O. Chyan, R. Ibrahim, G. Li, V. Mathew, A Cu–Cu wire-bonding enabled by a Cu-selective passivation coating to enhance packaging reliability, IEEE Trans. Compon. Packag. Manuf. Technol. 13 (12) (2023) 1923–1928.
[17] J. Chen, Y. Gong, Z.-G. Yang, Failure analysis on the pin fin heat sink for the power module of new energy vehicles, Eng. Fail. Anal. 143 (2023) 106870.
[18] Y. Wang, E. Deng, L. Wu, Y. Yan, Y. Zhao, Y. Huang, Influence of humidity on the power cycling lifetime of SiC MOSFETs, IEEE Trans. Compon. Packag. Manuf. Technol. 12 (11) (2022) 1781–1790.
[19] P. Singh, L. Palmer, M. Smith, D.S. Citrin, A. Locquet, D. Hampannavar, H. Fu, M. M. Khaw, K.L. Tan, C. Xu, J. Kaufman, M. Pudas, H. Schweigart, S. Strixner, M. R. Meier, C. Wang, H. Akbari, Comparing various test environments for conformal coating evaluation, International Conference on Electronics Packaging (ICEP) 2022 (2022) 89–90.
[20] Q. Zhao, X. Liu, H. Wang, Y. Zhu, Y. An, D. Yu, J. Qi, Research progress in corrosion protection technology for electronic components, Metals 13 (9) (2023) 1508.
[21] W. Chen, X. Liu, D. Hu, X. Liu, X. Zhu, X. Fan, G. Zhang, J. Fan, Unraveling the hydrogen sulfide aging mechanism on electrical-thermal–mechanical property degradation of sintered nanocopper interconnects used in power electronics packaging, Materials & Design 238 (2024) 112702.
[22] W. Chen, X. Liu, Z. Yang, D. Hu, X. Liu, X. Zhu, X. Fan, G. Zhang, J. Fan, Insights into sulfur and hydrogen sulfide induced corrosion of sintered nanocopper paste: a combined experimental and ab initio study, Mater. Des. 240 (2024) 112876.
[23] O.A. Bulavchenko, Z.S. Vinokurov, In situ X-ray diffraction as a basic tool to study oxide and metal oxide catalysts, Catalysts 13 (11) (2023).
[24] D.-P. Tran, T.-W. Lin, K.-C. Shie, C. Chen, Non-destructive micro analysis of electromigration failures in solder microbumps using 3D X-ray computed tomography, Mater Charact 194 (2022) 112404.
[25] D.N.G. Krishna, J. Philip, Review on surface-characterization applications of X-ray photoelectron spectroscopy (XPS): recent developments and challenges, Applied Surface Science Advances 12 (2022) 100332.
[26] T.E. Davies, H. Li, S. Bessette, R. Gauvin, G.S. Patience, N.F. Dummer, Experimental methods in chemical engineering: scanning electron microscopy and X-ray ultra-microscopy—SEM and XuM, Can. J. Chem. Eng. 100 (11) (2022) 3145–3159.
[27] G. Deng, C. Nagy, P. Yu, Combined molecular spectroscopic techniques (SR-FTIR, XRF, ATR-FTIR) to study physiochemical and nutrient profiles of Avena sativa grain and nutrition and structure interactive association properties, Crit. Rev. Food Sci. Nutr. 63 (25) (2023) 7225–7237.
[28] E. Buchan, M. Hardy, P.D.C. Gomes, L. Kelleher, H.O.M. Chu, P.G. Oppenheimer, Emerging Raman spectroscopy and saliva-based diagnostics: from challenges to applications, Appl. Spectrosc. Rev. 59 (1) (2022) 1–38.
[29] K.S. Banu, M. Lerma, S.U. Ahmed, J.L. Gardea-Torresdey, Hyperspectral microscopy-applications of hyperspectral imaging techniques in different fields of science: a review of recent advances, Applied Spectroscopy Reviews 29 (7) (2023) 1–24.
[30] P. Miao, N. Hao, Q. Zhao, J. Ping, C. Liu, Non-destructive determination of ginsenosides in ginseng by combined hyperspectral and X-ray techniques based on ensemble learning, Food Chem. 437 (2024) 137828.
[31] P. Ma, J. Li, Y. Zhuo, P. Jiao, G. Chen, Coating condition detection and assessment on the steel girder of a bridge through hyperspectral imaging, Coatings 13 (6) (2023) 1008.
[32] Z. Zahiri, A. Lamberti, J. Wielant, P. Scheunders, Characterization of corrosion products on carbon steel using hyperspectral imaging in Short-Wave Infrared (SWIR), in: 2022 12th Workshop on Hyperspectral Imaging and Signal Processing: Evolution in Remote Sensing (WHISPERS), 2022.
[33] T. De Kerf, G. Pipintakos, Z. Zahiri, S. Vanlanduit, P. Scheunders, Identification of corrosion minerals using shortwave infrared hyperspectral imaging, Sensors 22 (1) (2022) 406.
[34] M. Al Ktash, M. Stefanakis, T. Englert, M.S.L. Drechsel, J. Stiedl, S. Green, T. Jacob, B. Boldrini, E. Ostertag, K. Rebner, M. Brecht, UV hyperspectral imaging as process analytical tool for the characterization of oxide layers and copper states on direct bonded copper, Sensors 21 (21) (2021) s21217332.
[35] F. Liggins, A. Vichi, W. Liu, A. Hogg, S. Kogou, J. Chen, H. Liang, Hyperspectral imaging solutions for the non-invasive detection and automated mapping of copper trihydroxychlorides in ancient bronze, Herit. Sci. 10 (1) (2022) 142.
[36] J. Tao, Y. Gu, X. Hao, R. Liang, B. Wang, Z. Cheng, B. Yan, G. Chen, Combination of hyperspectral imaging and machine learning models for fast characterization and classification of municipal solid waste, Resour. Conserv. Recycl. 188 (2023) 106731.
[37] H. Pu, J. Yu, D.-W. Sun, Q. Wei, X. Shen, Z. Wang, Distinguishing fresh and frozen-thawed beef using hyperspectral imaging technology combined with convolutional neural networks, Microchem. J. 189 (2023) 108559.
[38] X. Zhou, C. Zhao, J. Sun, K. Yao, M. Xu, J. Cheng, Nondestructive testing and visualization of compound heavy metals in lettuce leaves using fluorescence hyperspectral imaging, Spectrochim. Acta A Mol. Biomol. Spectrosc. 291 (2023) 122337.
[39] Y. Unutulmazsoy, C. Cancellieri, M. Chiodi, S. Siol, L. Lin, L.P.H. Jeurgens, In situ oxidation studies of Cu thin films: growth kinetics and oxide phase evolution, J. Appl. Phys. 127 (6) (2020).
[40] C.L. Cheng, Shalabh, G. Garg, Coefficient of determination for multiple measurement error models, Journal of Multivariate Analysis 126 (2014) 137–152.